Radiology

ORIGINAL RESEARCH ■ MOLECULAR IMAGING

Detection of Stem Cell Transplant Rejection with Ferumoxytol MR Imaging:

Correlation of MR Imaging Findings with Those at Intravital Microscopy[1]

Heike E. Daldrup-Link, MD, PhD
Carmel Chan, PhD
Olga Lenkov, MS
Seyedmeghdad Taghavigarmestani, MD
Toktam Nazekati, PhD
Hossein Nejadnik, MD, PhD
Fanny Chapelin, MS
Aman Khurana, MD
Xinming Tong, PhD
Fan Yang, PhD
Laura Pisani, PhD
Michael Longaker, MD, PhD
Sanjiv Sam Gambhir, MD, PhD

Purpose: To determine whether endogenous labeling of macrophages with clinically applicable nanoparticles enables noninvasive detection of innate immune responses to stem cell transplants with magnetic resonance (MR) imaging.

Materials and Methods: Work with human stem cells was approved by the institutional review board and the stem cell research oversight committee, and animal experiments were approved by the administrative panel on laboratory animal care. Nine immunocompetent Sprague-Dawley rats received intravenous injection of ferumoxytol, and 18 Jax C57BL/6-Tg (Csf1r-EGFP-NGFR/FKBP1A/TNFRSF6) 2Bck/J mice received rhodamine-conjugated ferumoxytol. Then, 48 hours later, immune-matched or mismatched stem cells were implanted into osteochondral defects of the knee joints of experimental rats and calvarial defects of Jax mice. All animals underwent serial MR imaging and intravital microscopy (IVM) up to 4 weeks after surgery. Macrophages of Jax C57BL/6-Tg (Csf1r-EGFP-NGFR/FKBP1A/TNFRSF6) 2Bck/J mice express enhanced green fluorescent protein (GFP), which enables in vivo correlation of ferumoxytol enhancement at MR imaging with macrophage quantities at IVM. All quantitative data were compared between experimental groups by using a mixed linear model and *t* tests.

Results: Immune-mismatched stem cell implants demonstrated stronger ferumoxytol enhancement than did matched stem cell implants. At 4 weeks, T2 values of mismatched implants were significantly lower than those of matched implants in osteochondral defects of female rats (mean, 10.72 msec for human stem cells and 11.55 msec for male rat stem cells vs 15.45 msec for sex-matched rat stem cells; $P = .02$ and $P = .04$, respectively) and calvarial defects of recipient mice (mean, 21.7 msec vs 27.1 msec, respectively; $P = .0444$). This corresponded to increased recruitment of enhanced GFP– and rhodamine-ferumoxytol–positive macrophages into stem cell transplants, as visualized with IVM and histopathologic examination.

Conclusion: Endogenous labeling of macrophages with ferumoxytol enables noninvasive detection of innate immune responses to stem cell transplants with MR imaging.

Online supplemental material is available for this article.

[1] From the Department of Radiology, Molecular Imaging Program at Stanford (MIPS) (H.E.D.L., C.C., O.L., S.T., T.N., H.N., F.C., A.K., F.Y., L.P., M.L., S.S.G.), Department of Pediatrics (H.E.D.L.), Institute for Stem Cell Biology and Regenerative Medicine (H.E.D.L.), Department of Orthopaedic Surgery (X.T., F.Y.), Department of Bioengineering (F.Y., S.S.G.), Department of Surgery, Division of Plastic and Reconstructive Surgery (M.L.), and Department of Materials Science and Engineering (M.L., S.S.G.), Stanford University, 725 Welch Rd, Room 1665, Stanford, CA 94305-5614.
Received May 25, 2016; revision requested July 12; revision received October 19; accepted November 9; final version accepted November 16. **Address correspondence to** H.E.D. (e-mail: *H.E.Daldrup-Link@stanford.edu*).

Supported by the National Institute of Arthritis and Musculoskeletal and Skin Diseases (grant 2R01AR054458) and the Musculoskeletal Transplant Foundation (MTF) (Established Investigator Grant Award).

Stem cells can possess major and minor histocompatibility antigen incompatibilities, which can be recognized by the host immune system and lead to rejection (1–4). Although allogeneic mesenchymal stromal cells (MSCs) were initially thought to be immune privileged, evidence now suggests that MSCs are recognized and rejected by the immune system of histocompatibility antigen-mismatched hosts (5,6). Because the use of third party ("off the shelf") MSC transplants is advocated (7–13), and thus rejection may be a common occurrence, a noninvasive diagnostic test for in vivo detection of immune responses against cell transplants is critically needed to enable timely immune-modulating interventions. Immune rejection involves a complex crosstalk between transplanted stem cells and host immune cells (1,2,4,7,14–20). Contrary to T cell–mediated immune responses against solid organ transplants, immune rejection of stem cell transplants is typically initiated by the innate immune system (21). Monocytes and macrophages recognize "foreign" cell transplants and release inflammatory mediators such as reactive oxygen species, which leads to a vicious cycle of tissue inflammation, cell damage, and, ultimately, loss of the cell transplant (5,6). An imaging test that could depict these immune responses directly, noninvasively, and longitudinally in vivo would substantially improve our ability to support stem cell engraftment and achieve more successful tissue regeneration outcomes.

Previous studies involved preclinical imaging tools for the detection of immune responses to cell transplants, by tracking either the long-term fate of labeled stem cells (1,22,23) or the migration of T cells (24–26) or macrophages (27–32) into the transplant. We recently reported an immediately clinically translatable approach for tracking macrophage migration into stem cell transplants (28). The approach relied on intravenous injection of ferumoxytol nanoparticles, which are phagocytosed by macrophages in bone marrow and which can be detected with magnetic resonance (MR) imaging. After transplantation of unlabeled stem cells, MR imaging could help visualize recruitment of nanoparticle-labeled macrophages to the transplant (28). We hypothesized that this macrophage tracking technique could be used to detect immune rejection processes against stem cell transplants. Therefore, the purpose of our study was to evaluate whether endogenous labeling of macrophages with clinically applicable nanoparticles enables noninvasive detection of innate immune responses to stem cell transplants with MR imaging.

Advances in Knowledge

- Host immune responses against stem cell transplants can be detected with a noninvasive MR imaging technique in which intravenous ferumoxytol is used to label and track macrophages in vivo.
- Implantation of metal-free window chambers and injection of rhodamine-conjugated ferumoxytol enable combined MR imaging and in vivo microscopy studies, which can link real-time histopathologic findings with signal intensity changes at MR imaging.
- Injection of unmodified ferumoxytol labels only a fraction of existing macrophages.

Materials and Methods

MR imaging data for this study were analyzed with Cinetool Postprocessing Software, which was provided by Sandeep Gupta, PhD, from GE Research (Niskayuna, NY). Dr Gupta did not participate in data collection or analyses. The authors had complete control of the study data and the information submitted for publication.

Human MSCs were purchased from Lonza (Walkersville, Md, catalog no. PT-2501). Human adipose-derived stromal cells (ADSCs) were harvested from lipoaspirates of female patients (age range, 28–49 years) and isolated by means of a series of digestions by using type II collagenase as previously described (33,34). MSCs and ADSCs were used after no more than five passages. Work with human tissue was approved through the institutional review board (protocol 2188), and work with human ADSCs was approved by the stem cell research oversight committee (protocol 177).

Animal experiments were approved by the Stanford Administrative Panel on Laboratory Animal Care (protocols 27357, 24365, and 9999). All animals were treated in accordance with the National Research Council's Guide for the Care and Use of Laboratory Animals. All animal experiments were performed with the animal under isoflurane anesthesia. Buprenorphine treatment was used for pain control after surgeries.

The first set of experiments was carried out in an established rat model

Implications for Patient Care

- The described macrophage MR imaging approach could provide noninvasive information about stem cell engraftment or failure.
- The results could motivate administration of immune response modifiers to patients who show imaging signs of stem cell rejection.

https://doi.org/10.1148/radiol.2017161139

Content codes: MR MI

Radiology 2017; 284:495–507

Abbreviations:
ADSC = adipose-derived stem cell
GFP = green fluorescent protein
IVM = intravital microscopy
MSC = mesenchymal stromal cell

Author contributions:
Guarantors of integrity of entire study, H.E.D., O.L.; study concepts/study design or data acquisition or data analysis/interpretation, all authors; manuscript drafting or manuscript revision for important intellectual content, all authors; approval of final version of submitted manuscript, all authors; agrees to ensure any questions related to the work are appropriately resolved, all authors; literature research, H.E.D., C.C., O.L., S.T., T.N., H.N., F.C., M.L., S.S.G.; clinical studies, M.L.; experimental studies, H.E.D., C.C., O.L., S.T., T.N., H.N., F.C., A.K., X.T., L.P., M.L.; statistical analysis, O.L., S.T., T.N., M.L.; and manuscript editing, H.E.D., C.C., O.L., S.T., T.N., H.N., F.C., A.K., F.Y., L.P., M.L., S.S.G.

Conflicts of interest are listed at the end of this article.

See also Science to Practice in this issue.

of osteochondral defects of the knee joint (28): Nine female immunocompetent Sprague-Dawley rats received intravenous injection of ferumoxytol (Feraheme; Advanced Magnetics, Cambridge, Mass) at a dose of 0.5 mmol iron per kilogram of body weight. Ferumoxytol is a U.S. Food and Drug Administration–approved iron supplement composed of iron oxide nanoparticles that are phagocytosed by macrophages in liver, spleen, and bone marrow and which can be detected with MR imaging by means of a low (dark) signal intensity on T2-weighted MR images (35–37). At 48 hours after ferumoxytol administration, osteochondral defects were created in the bilateral femurs of injected rats and MSCs were implanted in these defects. Six knee defects received immune-matched female rat MSC implants, six received immune-mismatched male rat MSC implants (obtained from bone marrow aspirates of Sprague-Dawley rats as described previously [35]), and six received immune-mismatched human MSC implants. All stem cell implants were imaged with a 7.0-T MR unit (Discovery MR901; collaboration between Agilent [Santa Clara, Calif] and GE Healthcare [Waukesha, Wis]) by using a T2-weighted spin-echo sequence (repetition time msec/echo times msec, 4000/15, 30, 45, 60; number of signal acquired, one) at 0, 2, and 4 weeks after MSC implantation (Fig E1 [online]). T2 relaxation times were calculated by using custom-designed software (Cinetool, GE Research). Animals were then sacrificed and knees explanted and processed for histopathologic correlations.

To better understand the relationship between MR imaging signal intensity changes, iron oxide nanoparticle compartmentalization, and macrophage recruitment, we designed a novel mouse model for integrated MR imaging and intravital microscopy (IVM) studies of immune responses to stem cell transplants. The model relies on creation of 5-mm calvarial defects, which can be repaired by transplanting MSCs in growth factor–enriched scaffold (33,38,39). We used Jax C57BL/6-Tg (Csf1r-EGFP-NG-FR/FKBP1A/TNFRSF6) 2Bck/J mice, which express an enhanced green fluorescent protein (GFP) under the control of the Cftr1 promoter and thus have green fluorescent mononuclear cells, including macrophages, monocytes, and dendritic cells. We injected 18 mice with rhodamine-labeled ferumoxytol as an MR imaging–detectable macrophage marker (three doses of 0.5 mmol iron per kilogram of body weight over 5 days). Then, 48 hours later, we created calvarial defects and implanted 5×10^5 murine ADSCs (n = 9) or mismatched human ADSCs in alginate scaffold (n = 9) into these defects (40). The scaffold consisted of polyethylene glycol (molecular weight, 3000 Da) conjugated to dimethacrylate. The ammonium persulfate and tetramethylethylenediamine were used to catalyze the polymerization of acrylamide to form a polyacrylamide gel (Fig E2 [online]).

To confirm engraftment of matched cell transplants and lack of engraftment of mismatched cell transplants, nine pilot mice received luciferase-transfected murine ADSC transplants (n = 3), human ADSC transplants (n = 3), or scaffold-only transplants (n = 3) and underwent serial computed tomography (CT) and optical imaging studies after intravenous injection of D-luciferin (see details in Appendix E1 [online]). In addition, we confirmed the osteogenic differentiation potential of the murine and human ADSCs by culturing 6×10^4 cells per square centimeter in osteogenic differentiation media, which consisted of low glucose Dulbecco's modified Eagle's medium supplemented with 10% fetal bovine serum (Gibco, Langley, Okla), 100 U/mL penicillin, 100 μg/mL streptomycin (Gibco), 10% L-glutamine (Gibco), 50 μg/mL L-ascorbic acid 2-phosphate sequimagnesium (Sigma, Carlsbad, Calif), 100 mmol/L sodium pyrovate (Gibco), 0.1 μmol/L dexamethasone (Sigma), and 10 mmol/L b-glycerophosphate. Cells were harvested on day 21 and stained with Alizarin red S (Sigma-Aldrich, St Louis, Mo) for calcium deposits.

To compare MR imaging signal intensity changes with macrophage recruitment to cell transplants, we designed MR imaging–compatible window chambers consisting of a polyether ether ketone ring and a glass window, which were implanted above the cell transplants (Figs E3, E4 [online]). All implants were imaged with a 7.0-T animal MR unit at 1, 5, 10, 14, and 21 days after surgery by using the same T2-weighted spin-echo sequence described earlier.

Directly after each MR examination, IVM images were acquired with a microscope (IV-100; Olympus, Tokyo, Japan) by using Olympus UplanFL objectives and Olympus FluoView FV300 software. An argon laser at 488 nm, a diode-pumped solid-state laser at 561 nm (both from Melles Griot, Carlsbad, Calif), and a diode laser at 748 nm (Olympus) excited enhanced GFP, rhodamine, and AngioSense 750 (Perkin-Elmer, Boston, Mass), respectively. To collect the light from the aforementioned fluorophores simultaneously, custom-built dichroic filters (SDM-570 nm, SDM-630 nm, and SDM-750 nm) and emission filters (BA 505–550 nm, BA 585–615 nm, and BA 770 nm IF [Olympus]) were used. Time per pixel was set to 8–12.5 μsec, and voltage was set to 500–600 V. The objective was set to focus onto the center of the cranial window. Time-lapse images were acquired over 5–10 minutes by using a ×10 objective to assess the motility of the cells. The vertical regions of interest were defined areas with fluorescent signal within the transplant, and Z-stack images (vertical stacks) were acquired by optically sectioning through the transplant in 30-μm steps by using the ×10 objective (typically 10−20 sections per region), resulting in an imaging depth of 0.2–1.5 mm. The size of macrophages was determined with ImageJ software (National Institutes of Health; Bethedsda, Md) on the basis of the size distribution of GFP-positive cells in the field of view (Fig E5 [online]), and the number of GFP-positive cells, rhodamine-positive cells, and double-positive cells was counted on each Z stack and averaged for each transplant.

Quantitative MR imaging and IVM data from stem cell transplants were tested for significant differences over time by using a mixed linear model with a random effect for each rat knee

Figure 1

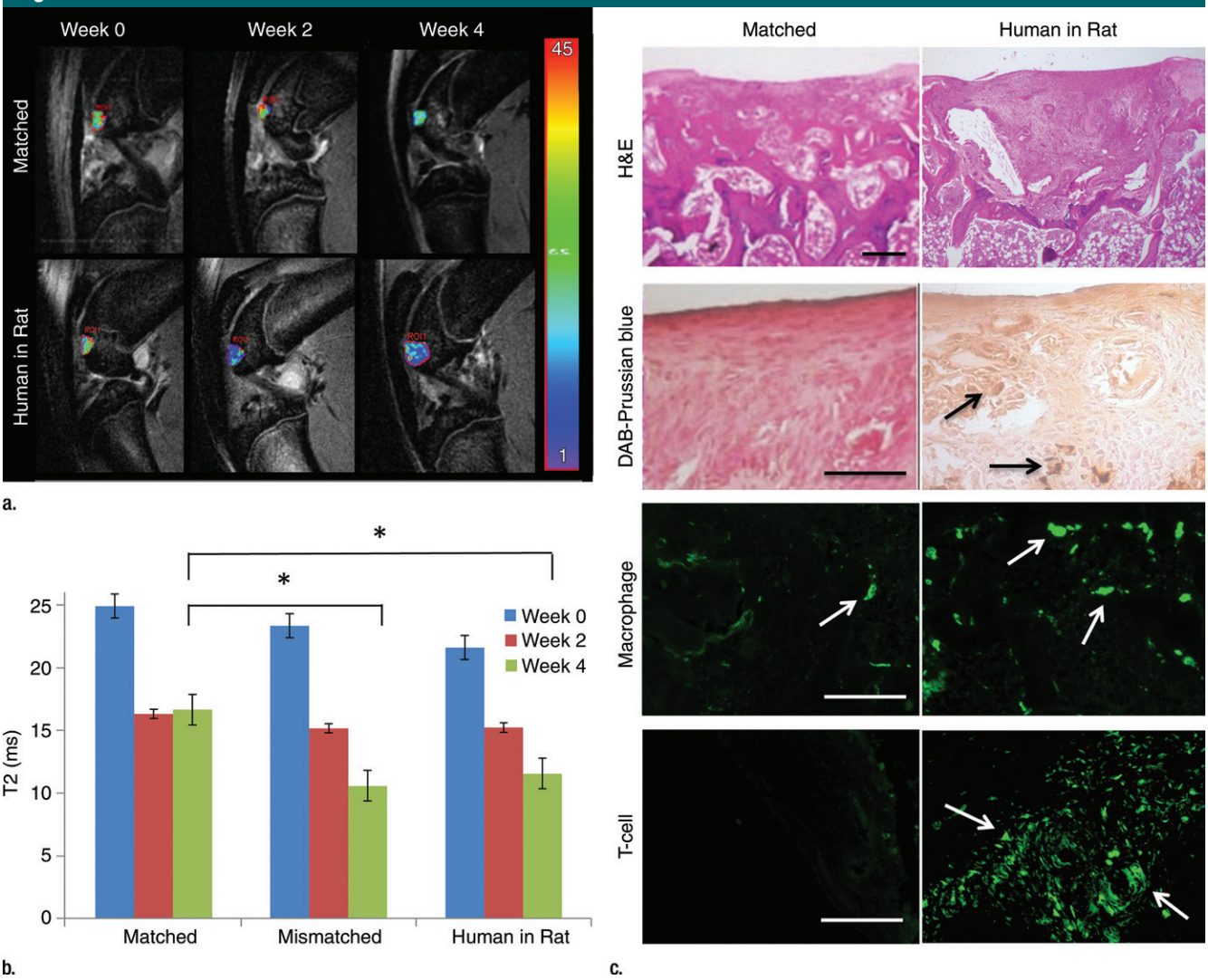

Figure 1: Noninvasive MR imaging detection of macrophage recruitment to stem cell implants in rat knee joints. **(a)** Sagittal T2-weighted fast spin-echo MR images (300/30) with superimposed T2 color maps of representative rat knee joints with matched stem cells (upper row) or mismatched MSC transplants (lower row) in osteochondral defects. **(b)** Chart shows corresponding T2 relaxation times of matched and mismatched stem cell transplants at different time points after stem cell implantation. Data are means and standard deviations of six transplants in each group. * = significant difference. **(c)** Corresponding photomicrographs. Matched transplants showed negative 3,3'-diaminobenzidine *(DAB)*–Prussian blue (iron), negative CD3 stains, and few CD68-positive macrophages while mismatched transplants exhibited strongly positive diaminobenzidine–Prussian blue and CD68 staining and presence of several CD3-positive T cells (arrows). *H&E* = hematoxylin-eosin. Bars = 200 μm.

or calvarial defect. Differences between matched and mismatched ADSC transplants were tested with a *t* test. The linear mixed model was used to analyze changes in quantitative values over time within each experimental group (matched, sex-mismatched, and species-mismatched transplants), whereas *t* tests were used to compare matched and mismatched transplants at specific time points. $P < .05$ was considered indicative of a statistically significant difference.

Results

Stem Cell Transplants in Osteochondral Defects of Rat Knee Joints

All stem cell transplants demonstrated hyperintense signal on T2-weighted MR images directly after implantation, apparently due to the high proton content of the scaffold. T2 relaxation times decreased significantly over time for all transplants (Figs 1, E1 [online]). The linear mixed model was fit by means of restricted maximum likelihood. The log likelihood was 93.601, 90.042, and 79.806; the Akaike information criterion was 101.601, 98.042, and 87.806; and the Bayesian information criterion was 104.691, 101.132, and 90.362 for

Figure 2

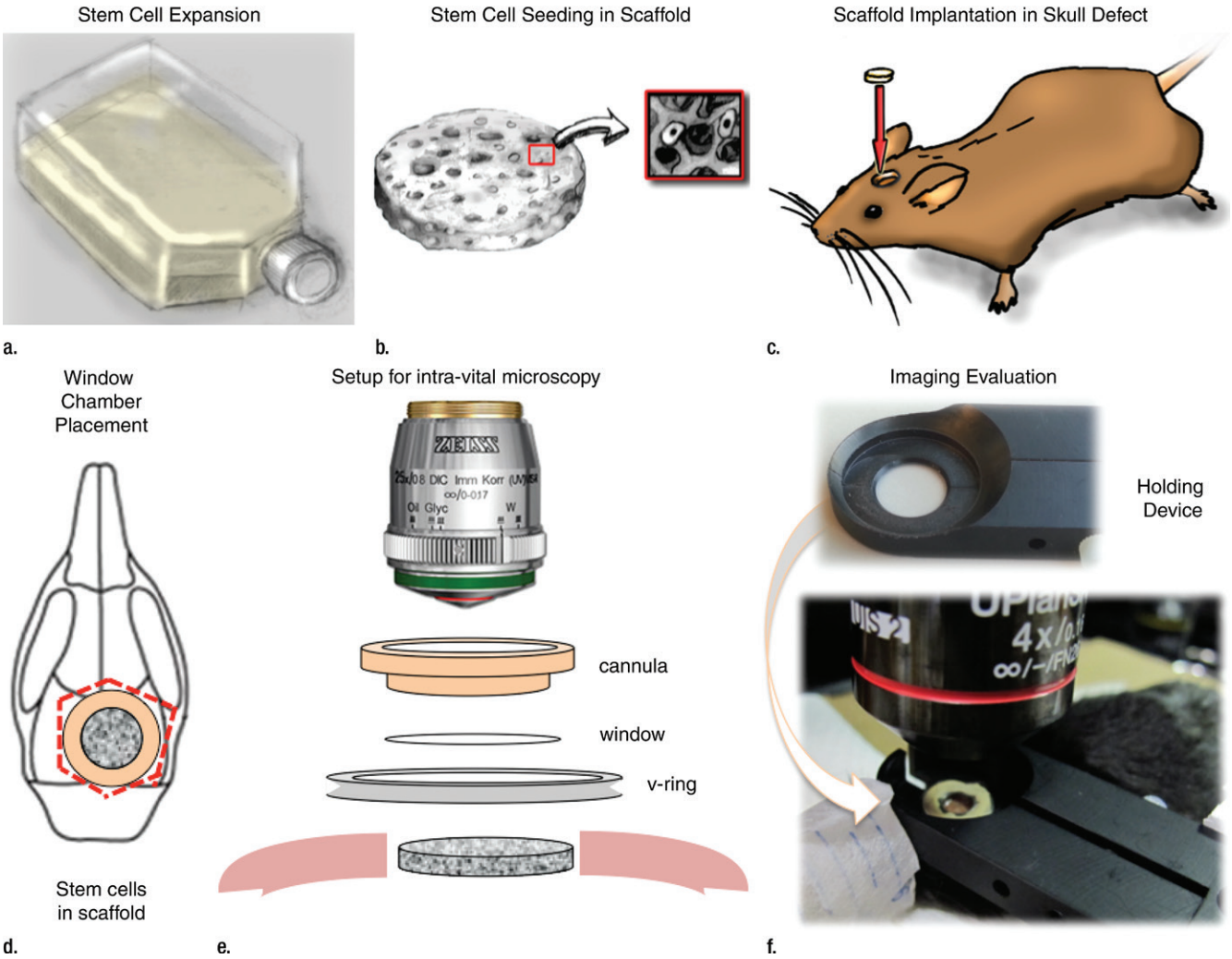

Figure 2: Experimental design for integrated MR imaging and IVM of cell transplants in calvarial defects. **(a)** ADSCs were expanded in cell culture. **(b)** ADSCs were seeded in scaffold. **(c)** ADSCs in scaffold were implanted in calvarial defects of recipient mice. **(d)** A custom-made MR imaging–compatible window chamber was implanted above scaffold. **(e)** A cannula was attached to window chamber for connection with a holding device. **(f)** Holding device was tailored to aperture of microscope and avoided motion artifacts during IVM sessions (see further details in Figs E1–E3 [online]).

matched, sex-mismatched, and species-mismatched (human) transplants, respectively. At 4 weeks after transplant, both sex-mismatched and human stem cell transplants showed significantly shorter T2 relaxation times (mean ± standard deviation, 10.72 msec ± 1.19 [P = .02] and 11.55 msec ± 1.3 [P = .04], respectively) compared with immune-matched transplants (mean, 15.45 msec ± 1.99 [P = .037]). Histopathologic correlations revealed increased quantities of Prussian blue–positive iron, CD68-positive macrophages, and CD3-positive T cells in mismatched transplants when compared with matched transplants (Figs 1, E1 [online]).

Stem Cell Transplants in Bone Defects of Mouse Calvaria

An overview of the technical design of our mouse model is shown in Figure 2, and details are shown in Figures E2–E5 (online). In vitro studies helped confirm that the applied ADSC formed bone (Fig E6 [online]), and pilot CT studies showed that there was no significant in vivo bone regeneration in the center of the defect during the early post-transplant period, up to 21 days after ADSC implantation (Fig E7 [online]). Because both ferumoxytol and mature bone cause low signal intensity on T2-weighted MR images, we wanted to exclude significant bone formation in the defect during our observation period as a potentially confounding variable. Results showed peripheral defect repair

Figure 3

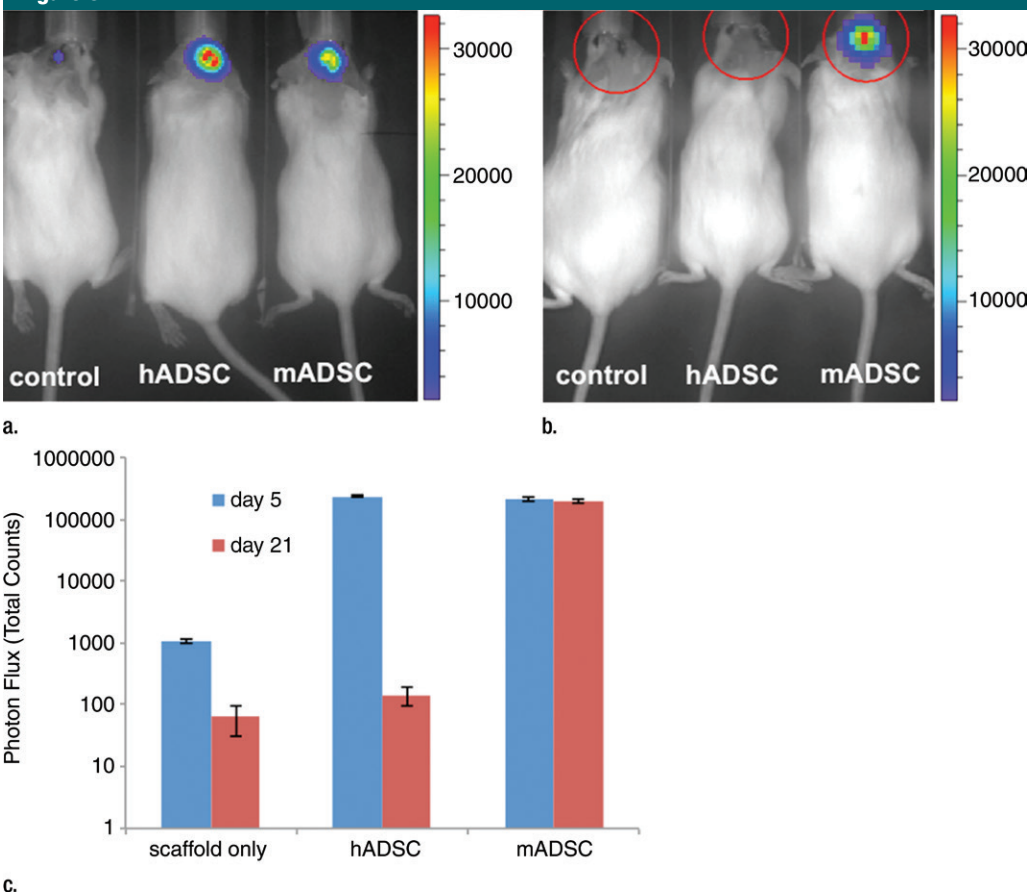

Figure 3: Bioluminescence imaging of matched and mismatched ADSC implants in calvarial defects. **(a, b)** Representative images obtained 3 (**a**) and 21 (**b**) days after implantation of luciferase-transfected murine ADSC *(mADSC)*, luciferase-transfected human ADSC *(hADSC)*, or scaffold only (control). Images were obtained with IVIS 200 system (PerkinElmer, Hopkinton, Mass) after intravenous injection of 15 mg/mL D-luciferin. **(c)** Chart shows corresponding bioluminescence imaging signal of implants during 1-second exposure time. Data are means and standard deviations of three implants in each group. Data were analyzed with living image software (Xenogen, PerkinElmer) by integrating the total photon flux emission (photons per second) within region of interest, normalized to background signal.

in animals with a matched transplant and no defect repair in animals with mismatched transplants (Fig E7 [online]). Serial luminescence images after implantation of luciferase-transfected ADSC showed persistent luminescence of murine but not human cell transplants during an observation time of 21 days, which confirms engraftment of murine ADSC but not human ADSC (Fig 3). Control mice with scaffold only showed no significant background signal intensity (Fig 3).

Accordingly, serial MR images of matched murine ADSC transplants demonstrated only a slight decrease in T2 signal intensity over time (Fig 4), whereas mismatched transplants showed a stronger decrease in MR imaging signal intensity at the internal, dura-facing edge of the transplant (Fig 5). This corresponded to a significant decrease in the T2 relaxation times of mismatched transplants over time (T2 = 33.7, 27.6, 23.0, 20.5, and 21.7 msec at 1, 5, 10, 14, and 21 days, respectively; P = .0129); the decrease in the T2 relaxation times in matched transplants was not significant (T2 = 35.2, 33.0, 27.5, 26.9, and 27.1 msec; P = .1052). At 21 days after transplantation, the T2 relaxation times of mismatched transplants (mean, 21.7 msec ± 1.9) were significantly lower than those of the matched transplants (mean, 27.1 msec ± 1.0) (P = .0444) (Figs 6, 7).

Corresponding IVM studies demonstrated an increasing accumulation of GFP-positive macrophages in both matched and mismatched ADSC transplants over time (Figs 4–6). Mismatched transplants showed peak macrophage quantities at day 14, with a significantly higher mean quantity of macrophages (mean, 697 ± 52) compared with matched transplants (mean, 405 ± 59) (P = .0498) (Fig 7). This corresponded to the stronger

Figure 4

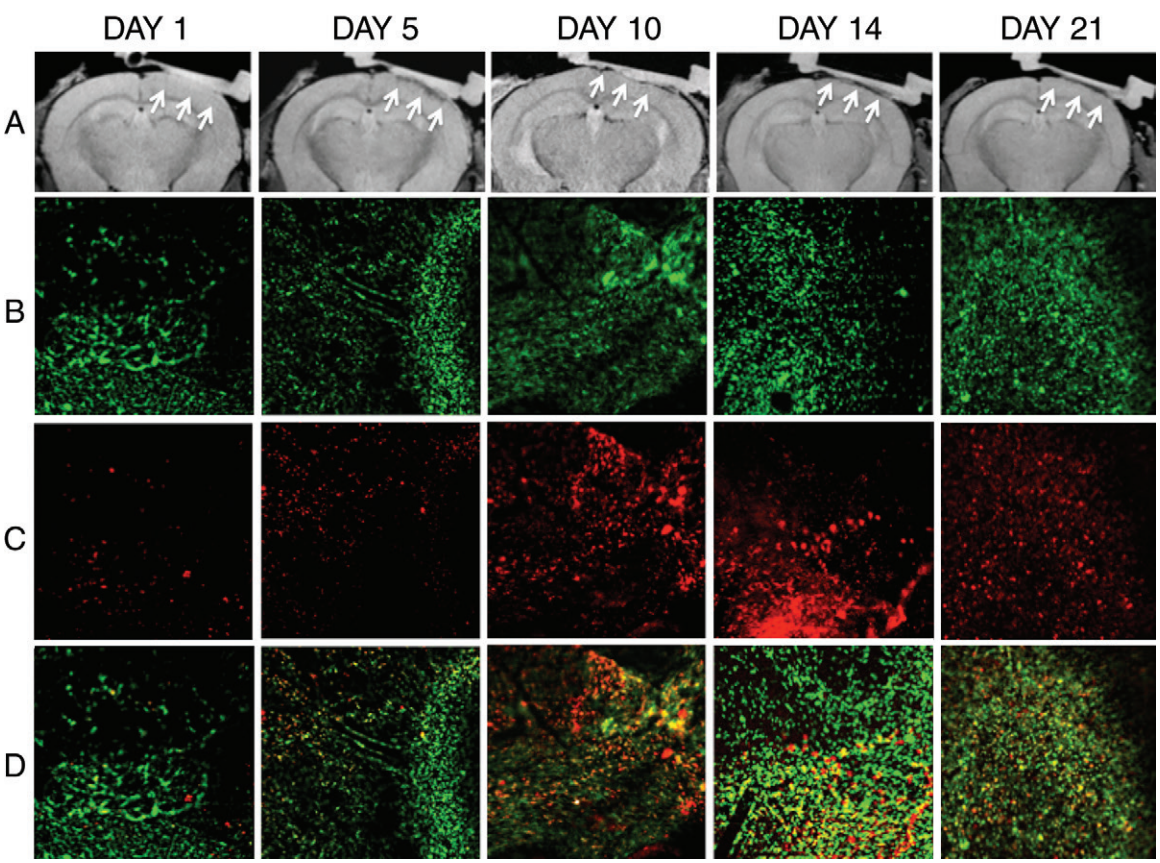

Figure 4: Representative images from MR imaging and IVM of matched ADSCs in calvarial defect of transgenic mouse, which has intrinsic GFP-expressing macrophages and which was injected with rhodamine-conjugated iron oxide nanoparticles (ferumoxytol). *A*, Coronal T2-weighted fast spin-echo MR images (3000/30) of matched murine ADSC implant (arrows) show minimal decrease in T2 signal intensity over time. *B*, Optical images with GFP filter show corresponding accumulation of green fluorescent cells in transplant. *C*, Optical images with rhodamine filter show corresponding accumulation of red fluorescent cells, which contain rhodamine-labeled ferumoxytol nanoparticles. *D*, Overlay of images in *B* and *C* shows that most rhodamine-labeled cells are also GFP positive (exhibiting yellow color), which indicates that rhodamine-ferumoxytol label localizes to macrophages.

T2 signal seen in human ADSC transplants at MR imaging.

There were fewer rhodamine-positive macrophages than GFP-positive macrophages in both groups (Figs 4–7); that is, not all macrophages were labeled by the clinical marker ferumoxytol. However, 90.1% of the rhodamine-positive cells were also GFP positive, which indicates that the ferumoxytol label was fairly specific for mononuclear cells. Only 9.9% of red fluorescent cells did not show green fluorescence. Increasing accumulations of GFP-positive macrophages in mismatched transplants compared with matched transplants correlated with increasing quantities of rhodamine-positive macrophages and increasing double-labeled macrophages; that is, even though rhodamine-conjugated ferumoxytol nanoparticles did not label all macrophages, the MR imaging–detectable fraction of ferumoxytol-labeled macrophages represented the overall macrophage population.

Discussion

Our data showed that stem cell transplant rejection can be diagnosed with MR imaging by detecting recruitment of iron oxide nanoparticle–labeled macrophages to the transplant. This potentially readily clinically translatable imaging approach could be used to evaluate immune responses to stem cell transplants noninvasively and repetitively in patients. This is important as, contrary to solid organ transplants, most stem cell transplants cannot be sampled for biopsy owing to their small size (eg, in cartilage defects), because of biomechanical reasons (eg, stability of a healing bone defect), or because of their critical location (eg, in the brain or around vessels).

Bone injuries are among the most costly and debilitating to individuals and our society (8,10,41,42). They are most commonly seen as a result

Figure 5

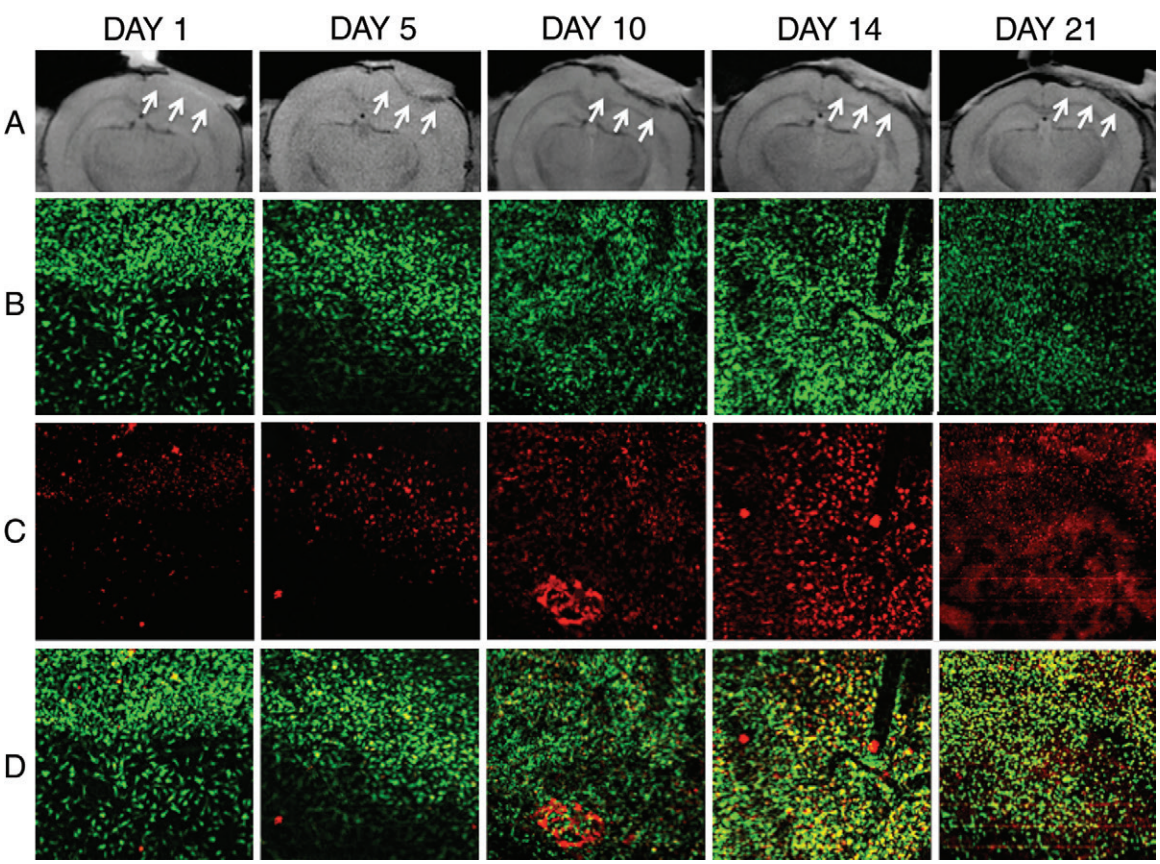

Figure 5: Representative images from MR imaging and IVM of mismatched ADSCs in calvarial defect of transgenic mouse, which has intrinsic GFP-expressing macrophages and which was injected with rhodamine-conjugated iron oxide nanoparticles (ferumoxytol). *A*, Coronal T2-weighted fast spin-echo images (3000/30) of mismatched human ADSC implant (arrows) show marked decrease in T2 signal intensity over time, apparently due to accumulation of ferumoxytol nanoparticles in transplant. *B*, Optical images with GFP filter show corresponding accumulation of green fluorescent cells in transplant. *C*, Optical images with rhodamine filter show accumulation of rhodamine-labeled cells. *D*, Overlay of images from *B* and *C* shows that rhodamine-labeled cells co-localize to GFP-positive cells (exhibiting yellow color).

of osteoarthritis, trauma, or tumor surgery and often do not heal without substantial medical intervention. More than 2 000 000 bone grafts are transplanted every year to provide support, fill voids, and enhance repair of bone defects, thereby representing the second most commonly transplanted material after blood product transplantations (43). Considering escalating demands and limited availabilities and efficacies of bone grafts, stem cell transplants represent an attractive alternative to bone repair (44). Bone allografts must be processed to avoid transmitting diseases from the donor to the patient, leaving the bone sterile but dead. Bone allografts lack living cells that could help the implant better integrate with existing bone. As a consequence, they provide incomplete repair or break within a year in up to 30% of patients (43). Stem cells represent "live" sources for bone engineering and have many advantages, including higher tissue regeneration potential, immediate availability, potentially unlimited quantities, and generally better engraftment outcomes (8,10,41,42).

"Off the shelf" allogeneic stem cells represent the most common source of stem cells for clinical transplantations. However, allogeneic adult stem cells (1,3,4,45), embryonic stem cell–derived progenitors (16,19,46–48), and even autologous induced pluripotent stem cells, or iPS cells (14,20), can possess major and minor histocompatibility antigen differences, which can be recognized as foreign by the host immune system and lead to their rejection. Macrophages play a major role in immune responses to stem cell transplants (5). The underlying tissue injury initiates the production of damage-associated molecular patterns, which leads to activation of the complement system and recruitment and activation of innate immune cells (49). Our data showed that we can detect this immune response with a noninvasive MR imaging technique. Our macrophage marker ferumoxytol has the distinct advantage over

Figure 6

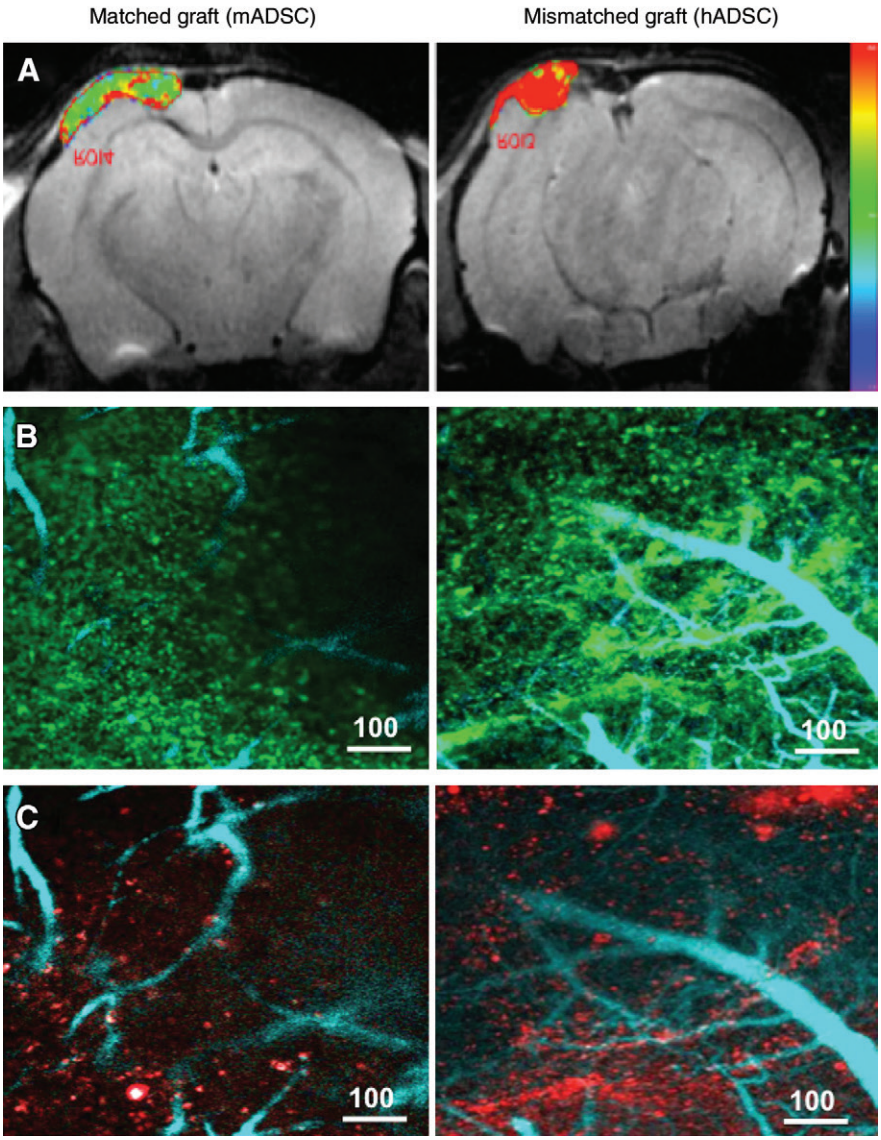

Figure 6: Comparative MR and IVM images of matched and mismatched ADSC implants in calvarial defects of transgenic mice. *A*, Coronal T2-weighted fast spin-echo images (3000/30) with superimposed R2 (1/T2) color maps show stronger R2 enhancement of mismatched compared with matched ADSC transplants in calvarial defects. *B*, Corresponding IVM images with GFP and AngioSense 750 filter show more GFP-positive macrophages in mismatched compared with matched transplants. *C*, Corresponding IVM images with rhodamine and AngioSense 750 filter show more rhodamine-positive macrophages in mismatched compared with matched transplants. GFP- and rhodamine-positive cells localize to extravascular space.

previously described cell labels that it is approved by the U.S. Food and Drug Administration as an iron supplement and, thus, immediately clinically available via an "off-label" use (36,37,50,51). By injecting ferumoxytol nanoparticles before stem cell transplantation, we achieved intrinsic macrophage labeling and high specificity of our MR imaging approach for macrophage imaging. Intravenous ferumoxytol administration after stem cell implantation would have led to nanoparticle accumulation in microvessels, the interstitium (52), macrophages (35), and mesenchymal stromal cells (35,53) in the transplant, reducing the specificity of our MR imaging approach.

The blood half-life of ultrasmall superparamagnetic iron oxide particles differs in humans and rodents. The blood half-life of ultrasmall superparamagnetic iron oxide particles with a hydrodynamic diameter of 30–40 nm is about 2 hours in rats and 24–36 hours in humans (54). In rats, increasing the dose significantly prolonged the blood half-life (54). Because the access of iron oxide nanoparticles to macrophages is favored by prolonged blood residence time, animal imaging experiments are generally performed by using high doses of ultrasmall superparamagnetic iron oxide particles (200–1000 mmol iron per kilogram body weight) compared with clinical doses (54). Therefore, we administered a high ferumoxytol dose of 0.5 mmol iron per kilogram body weight on 3 days (3 × 28 mg iron per kilogram body weight or 1.68 mg iron total to a 20-g mouse). By comparison, a patient receives a U.S. Food and Drug Administration–approved dose of 2 × 510 mg, or 1020 mg iron per 70-kg patient (14.5 mg iron per kilogram body weight). Future studies must determine if the human dose is sensitive enough for in vivo macrophage tracking.

Numerous preclinical and clinical studies have shown that intravenously injected ferumoxytol is phagocytosed by macrophages in vivo (28,37,55–57). Ferumoxytol uptake in the liver is seen as early as 10 minutes after its intravenous administration (36). Our studies showed that rhodamine-ferumoxytol–labeled macrophages can be tracked in vivo with both MR imaging and IVM. However, our data also showed that ferumoxytol labels only a fraction of the overall macrophage population. This is in accordance with previous reports that showed that certain macrophage-like cells are not labeled with unmodified nanoparticles (58) and that the shape and chemical properties of nanoparticles can influence nanoparticle uptake into specific macrophage

Figure 7

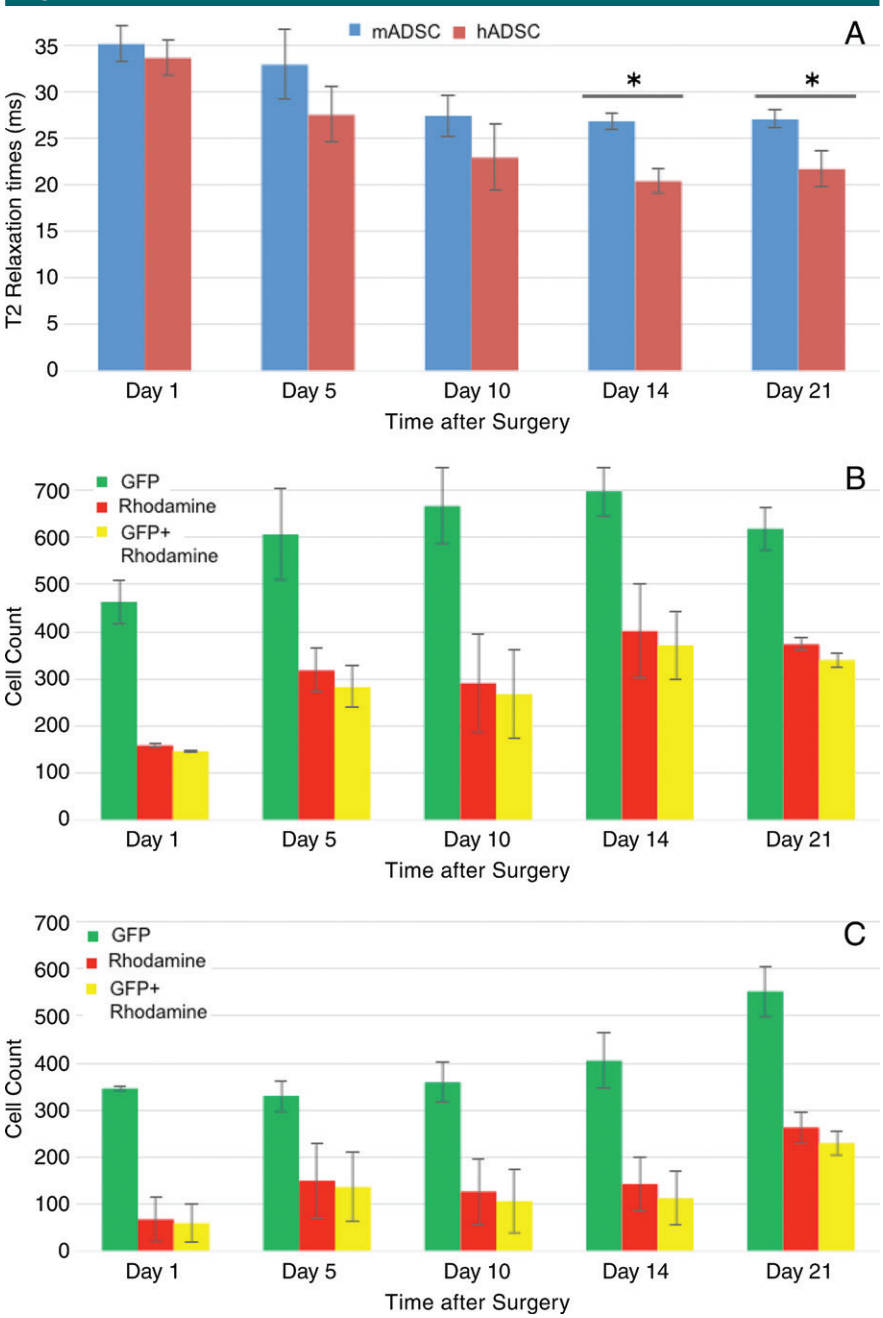

Figure 7: Bar charts show corresponding quantitative MR imaging and IVM data at different time points after implantation of matched and mismatched ADSC implants into calvarial defects. *A*, T2 relaxation times of mismatched human ADSC *(hADSC)* implants in mice preinjected with ferumoxytol are significantly shorter than those in mice with matched murine ADSC *(mADSC)*. * = significant difference. *B*, Macrophage counts in mismatched human ADSC implants on IVM images reveal parallel increase in both GFP- and rhodamine-labeled macrophages. *C*, Macrophage counts in matched murine ADSC implants on IVM images show recruitment of fewer GFP- and rhodamine-labeled macrophages compared with that in *B*. All data are means and standard deviations from six animals in each group.

subtypes (59). Further studies must show if modification of ferumoxytol can provide higher yield or more specific macrophage labeling. The advantage of using unmodified ferumoxytol is its immediate clinical applicability.

A limitation of the preinjection technique is that it can only be applied during the first 3 weeks after cell transplantation. However, this time window aligns well with acute rejection processes of allogeneic cell transplants (5,6). Alternatively, we can detect graft failure by labeling the transplanted stem cells (60,61). This requires ex vivo iron labeling for allogeneic cell transplants and knowledge of cell-specific proliferation and iron dilution, exocytosis, and metabolization processes. Combinations of our macrophage tracking technique with imaging markers of cell death (62) or other markers for T cells (63–65) and proinflammatory enzymes and cytokines (66–68) could further elucidate the timing between stem cell death and macrophage recruitment and elucidate the event cascade that leads to graft failure and, thereby, help us develop more successful cell therapies.

We did not prove the origin of the iron oxide–loaded macrophages, which migrated into stem cell transplants. In our knee model, it is most likely that bone marrow macrophages migrated from the adjacent bone marrow into osteochondral defects. However, we cannot exclude that macrophages from other organs, particularly the spleen, may have migrated into our implants. Neither our MR imaging technique nor histopathologic techniques available to us can enable the differentiation between macrophages that originated from bone marrow, spleen, or liver. With regard to the diagnosis of immune rejection processes, the origin of the observed macrophage influx may be of academic interest but does not seem to be clinically important.

Our study builds on our extensive experience with evaluations of iron oxide nanoparticles as MR contrast agents in phase II and III clinical trials during the past 2 decades (69–77). These agents are generally well tolerated and

show excellent safety profiles overall (51,69,73,78). The delivered dose through a typical iron oxide administration in patients is on the order of 2–5 mg iron per kilogram body weight (note that these are coated iron particles, not free iron), which is equivalent to or less than the iron dose administered with one blood transfusion. Iron oxide nanoparticles are slowly metabolized by the reticuloendothelial system and not excreted via the kidneys (78). Thus, they represent an alternative to gadolinium chelates for MR contrast enhancement in patients with renal insufficiency. However, the U.S. Food and Drug Administration has issued a black box warning for the use of ferumoxytol because severe anaphylactic reactions have been reported in response to ferumoxytol and other iron oxides, with an incidence of 0.1%–0.2% (78–80). Although these reactions are very rare, our ongoing studies are designed to develop a predictive blood test to determine an individual patient's risk of developing an allergic reaction to ferumoxytol.

Therapy implications are as follows: Patients who receive "off the shelf" major histocompatibility–unmatched allogeneic ADSC or MSC transplants do not currently receive immunosuppressive therapy because these cells were considered immune privileged and might even alleviate host immune responses (81). However, it has been recognized that MSCs represent a heterogeneous cell population with a wide spectrum of phenotypes and functional properties, some of which can activate innate immune responses (81). Our imaging test could help to better understand immune responses to different types of therapeutic cells or scaffolds and enable monitoring of immune-modulating interventions. For example, we noted substantially less T2 signal intensity changes of sex-mismatched cell transplants in athymic recipients in a previous study (28) compared with sex-mismatched cell transplants in immune competent recipients in the current study, which suggests the possibility of imaging different degrees of host immune responses. If clinical imaging studies reveal macrophage responses to allogeneic ADSC and MSC transplants in patients, then this might motivate concomitant immune suppression or renewed focus on autologous cell transplants.

In summary, we developed a clinically translatable imaging approach for diagnosing innate immune responses to cell transplants. This imaging test may be helpful for diagnosing stem cell transplant rejection early enough to initiate immune-modulating therapies and save the transplant. This imaging approach might also be useful to better understand and alleviate in vivo host immune response to different stem cell types (human embryonic stem cells, human MSC, human induced pluripotent stem cells), genetically engineered stem cells, and different scaffolds and growth factors.

Acknowledgments: We thank Sandeep Gupta, PhD, from GE Healthcare for providing image postprocessing software (Cinetool) for generating T2 maps. We thank the small animal imaging facility at Stanford for providing the equipment and infrastructure for this project.

Disclosures of Conflicts of Interest: H.D. disclosed no relevant relationships. **C.C.** disclosed no relevant relationships. **O.L.** disclosed no relevant relationships. **S.T.** disclosed no relevant relationships. **T.N.** disclosed no relevant relationships. **H.N.** disclosed no relevant relationships. **F.C.** disclosed no relevant relationships. **A.K.** disclosed no relevant relationships. **X.T.** disclosed no relevant relationships. **F.Y.** disclosed no relevant relationships. **L.P.** disclosed no relevant relationships. **M.L.** disclosed no relevant relationships. **S.S.G.** Activities related to the present article: disclosed no relevant relationships. Activities not related to the present article: received personal fees from Bracco Diagnostics, Cellsight Technologies, Endra, Gamma Medica, Grail, ImagAb, PureTech, Vave Health, Verily, VisualSonics, and Infinitus (China); has stock in Cellsight Technologies, Click Diagnostics, CytomX Therapeutics, Endra, Gamma Medica, Grail, ImaginAb, MagArray, NinePoint Medical, PureTech, RefleXion Medical, Rio Imaging, Spectrum Dynamics, and Vave Health. Other relationships: disclosed no relevant relationships.

References

1. Zangi L, Margalit R, Reich-Zeliger S, et al. Direct imaging of immune rejection and memory induction by allogeneic mesenchymal stromal cells. Stem Cells 2009; 27(11):2865–2874.
2. Karabekian Z, Posnack NG, Sarvazyan N. Immunological barriers to stem-cell based cardiac repair. Stem Cell Rev 2011;7(2):315–325.
3. Preynat-Seauve O, Krause KH. Stem cell sources for regenerative medicine: the immunological point of view. Semin Immunopathol 2011;33(6):519–524.
4. Yang XF. Immunology of stem cells and cancer stem cells. Cell Mol Immunol 2007;4(3):161–171.
5. English K, Wood KJ. Mesenchymal stromal cells in transplantation rejection and tolerance. Cold Spring Harb Perspect Med 2013;3(5):a015560.
6. Griffin MD, Ryan AE, Alagesan S, Lohan P, Treacy O, Ritter T. Anti-donor immune responses elicited by allogeneic mesenchymal stem cells: what have we learned so far? Immunol Cell Biol 2013;91(1):40–51.
7. Charron D, Suberbielle-Boissel C, Al-Daccak R. Immunogenicity and allogenicity: a challenge of stem cell therapy. J Cardiovasc Transl Res 2009;2(1):130–138.
8. Ciapetti G, Granchi D, Baldini N. The combined use of mesenchymal stromal cells and scaffolds for bone repair. Curr Pharm Des 2012;18(13):1796–1820.
9. Jorgensen C, Noël D. Mesenchymal stem cells in osteoarticular diseases. Regen Med 2011;6(6 Suppl):44–51.
10. Chimutengwende-Gordon M, Khan WS. Advances in the use of stem cells and tissue engineering applications in bone repair. Curr Stem Cell Res Ther 2012;7(2):122–126.
11. Zhang ZY, Teoh SH, Hui JH, Fisk NM, Choolani M, Chan JK. The potential of human fetal mesenchymal stem cells for off-the-shelf bone tissue engineering application. Biomaterials 2012;33(9):2656–2672.
12. Sherman LS, Munoz J, Patel SA, Dave MA, Paige I, Rameshwar P. Moving from the laboratory bench to patients' bedside: considerations for effective therapy with stem cells. Clin Transl Sci 2011;4(5):380–386.
13. Polak JM, Mantalaris S. Stem cells bioprocessing: an important milestone to move regenerative medicine research into the clinical arena. Pediatr Res 2008;63(5):461–466.
14. Boyd AS, Rodrigues NP, Lui KO, Fu X, Xu Y. Concise review: immune recognition of induced pluripotent stem cells. Stem Cells 2012;30(5):797–803.
15. Duffy MM, Ritter T, Ceredig R, Griffin MD. Mesenchymal stem cell effects on T-cell effector pathways. Stem Cell Res Ther 2011;2(4):34.
16. English K, Wood KJ. Immunogenicity of embryonic stem cell–derived progenitors af-

ter transplantation. Curr Opin Organ Transplant 2011;16(1):90–95.

17. Heidt S, Segundo DS, Chadha R, Wood KJ. The impact of Th17 cells on transplant rejection and the induction of tolerance. Curr Opin Organ Transplant 2010;15(4):456–461.
18. Kofidis T, de Bruin JL, Yamane T, et al. Stimulation of paracrine pathways with growth factors enhances embryonic stem cell engraftment and host-specific differentiation in the heart after ischemic myocardial injury. Circulation 2005;111(19):2486–2493.
19. Swijnenburg RJ, Tanaka M, Vogel H, et al. Embryonic stem cell immunogenicity increases upon differentiation after transplantation into ischemic myocardium. Circulation 2005;112(9 Suppl):I166–I172.
20. Zhao T, Zhang ZN, Rong Z, Xu Y. Immunogenicity of induced pluripotent stem cells. Nature 2011;474(7350):212–215.
21. Nilsson B, Korsgren O, Lambris JD, Ekdahl KN. Can cells and biomaterials in therapeutic medicine be shielded from innate immune recognition? Trends Immunol 2010;31(1):32–38.
22. Swijnenburg RJ, Schrepfer S, Cao F, et al. In vivo imaging of embryonic stem cells reveals patterns of survival and immune rejection following transplantation. Stem Cells Dev 2008;17(6):1023–1029.
23. Kim DE, Tsuji K, Kim YR, et al. Neural stem cell transplant survival in brains of mice: assessing the effect of immunity and ischemia by using real-time bioluminescent imaging. Radiology 2006;241(3):822–830.
24. Negrin RS, Contag CH. In vivo imaging using bioluminescence: a tool for probing graft-versus-host disease. Nat Rev Immunol 2006;6(6):484–490.
25. Cahalan MD. Imaging transplant rejection: a new view. Nat Med 2011;17(6):662–663.
26. Celli S, Albert ML, Bousso P. Visualizing the innate and adaptive immune responses underlying allograft rejection by two-photon microscopy. Nat Med 2011;17(6):744–749.
27. Christen T, Nahrendorf M, Wildgruber M, et al. Molecular imaging of innate immune cell function in transplant rejection. Circulation 2009;119(14):1925–1932.
28. Khurana A, Nejadnik H, Gawande R, et al. Intravenous ferumoxytol allows noninvasive MR imaging monitoring of macrophage migration into stem cell transplants. Radiology 2012;264(3):803–811.
29. Hitchens TK, Ye Q, Eytan DF, Janjic JM, Ahrens ET, Ho C. 19F MRI detection of acute allograft rejection with in vivo perfluorocarbon labeling of immune cells. Magn Reson Med 2011;65(4):1144–1153.
30. Goulet JL, Griffiths RC, Ruiz P, et al. Deficiency of 5-lipoxygenase accelerates renal allograft rejection in mice. J Immunol 2001;167(11):6631–6636.
31. Kanno S, Wu YJ, Lee PC, et al. Macrophage accumulation associated with rat cardiac allograft rejection detected by magnetic resonance imaging with ultrasmall superparamagnetic iron oxide particles. Circulation 2001;104(8):934–938.
32. Zhang Y, Dodd SJ, Hendrich KS, Williams M, Ho C. Magnetic resonance imaging detection of rat renal transplant rejection by monitoring macrophage infiltration. Kidney Int 2000;58(3):1300–1310.
33. Hyun J, Grova M, Nejadnik H, et al. Enhancing in vivo survival of adipose-derived stromal cells through Bcl-2 overexpression using a minicircle vector. Stem Cells Transl Med 2013;2(9):690–702.
34. Lo DD, Hyun JS, Chung MT, et al. Repair of a critical-sized calvarial defect model using adipose-derived stromal cells harvested from lipoaspirate. J Vis Exp 2012;(68):4221.
35. Khurana A, Chapelin F, Beck G, et al. Iron administration before stem cell harvest enables MR imaging tracking after transplantation. Radiology 2013;269(1):186–197.
36. Klenk C, Gawande R, Uslu L, et al. Ionising radiation-free whole-body MRI versus (18)F-fluorodeoxyglucose PET/CT scans for children and young adults with cancer: a prospective, non-randomised, single-centre study. Lancet Oncol 2014;15(3):275–285.
37. Aghighi M, Golovko D, Ansari C, et al. Imaging tumor necrosis with ferumoxytol. PLoS One 2015;10(11):e0142665.
38. Levi B, Nelson ER, Li S, et al. Dura mater stimulates human adipose–derived stromal cells to undergo bone formation in mouse calvarial defects. Stem Cells 2011;29(8):1241–1255.
39. Hyun JS, Tran MC, Wong VW, et al. Enhancing stem cell survival in vivo for tissue repair. Biotechnol Adv 2013;31(5):736–743.
40. Valente JF, Valente TA, Alves P, Ferreira P, Silva A, Correia IJ. Alginate based scaffolds for bone tissue engineering. Mater Sci Eng C 2012;32(8):2596–2603.
41. Brooks PM. Impact of osteoarthritis on individuals and society: how much disability? Social consequences and health economic implications. Curr Opin Rheumatol 2002;14(5):573–577.
42. Jorgensen C, Gordeladze J, Noel D. Tissue engineering through autologous mesenchymal stem cells. Curr Opin Biotechnol 2004;15(5):406–410.
43. Campana V, Milano G, Pagano E, et al. Bone substitutes in orthopaedic surgery: from basic science to clinical practice. J Mater Sci Mater Med 2014;25(10):2445–2461.
44. Undale AH, Westendorf JJ, Yaszemski MJ, Khosla S. Mesenchymal stem cells for bone repair and metabolic bone diseases. Mayo Clin Proc 2009;84(10):893–902.
45. O'Sullivan ES, Vegas A, Anderson DG, Weir GC. Islets transplanted in immunoisolation devices: a review of the progress and the challenges that remain. Endocr Rev 2011;32(6):827–844.
46. Thompson HL, Manilay JO. Embryonic stem cell–derived hematopoietic stem cells: challenges in development, differentiation, and immunogenicity. Curr Top Med Chem 2011;11(13):1621–1637.
47. Swijnenburg RJ, van der Bogt KE, Sheikh AY, Cao F, Wu JC. Clinical hurdles for the transplantation of cardiomyocytes derived from human embryonic stem cells: role of molecular imaging. Curr Opin Biotechnol 2007;18(1):38–45.
48. van der Bogt KE, Swijnenburg RJ, Cao F, Wu JC. Molecular imaging of human embryonic stem cells: keeping an eye on differentiation, tumorigenicity and immunogenicity. Cell Cycle 2006;5(23):2748–2752.
49. Eltzschig HK, Eckle T. Ischemia and reperfusion: from mechanism to translation. Nat Med 2011;17(11):1391–1401.
50. Iv M, Telischak N, Feng D, Holdsworth SJ, Yeom KW, Daldrup-Link HE. Clinical applications of iron oxide nanoparticles for magnetic resonance imaging of brain tumors. Nanomedicine (Lond) 2015;10(6):993–1018.
51. Muehe AM, Feng D, von Eyben R, et al. Safety report of ferumoxytol for magnetic resonance imaging in children and young adults. Invest Radiol 2016;51(4):221–227.
52. Nejadnik H, Castillo R, Daldrup-Link HE. Magnetic resonance imaging and tracking of stem cells. Methods Mol Biol 2013;1052:167–176.
53. Khurana A, Nejadnik H, Chapelin F, et al. Ferumoxytol: a new, clinically applicable label for stem-cell tracking in arthritic joints with MRI. Nanomedicine (Lond) 2013;8(12):1969–1983.
54. Corot C, Petry KG, Trivedi R, et al. Macrophage imaging in central nervous system and in carotid atherosclerotic plaque using ultrasmall superparamagnetic iron oxide in magnetic resonance imaging. Invest Radiol 2004;39(10):619–625.

55. Simon GH, von Vopelius-Feldt J, Fu Y, et al. Ultrasmall supraparamagnetic iron oxide–enhanced magnetic resonance imaging of antigen-induced arthritis: a comparative study between SHU 555 C, ferumoxtran-10, and ferumoxytol. Invest Radiol 2006;41(1):45–51.

56. McConnell HL, Schwartz DL, Richardson BE, Woltjer RL, Muldoon LL, Neuwelt EA. Ferumoxytol nanoparticle uptake in brain during acute neuroinflammation is cell-specific. Nanomedicine (Lond) 2016;12(6):1535–1542.

57. Weissleder R, Nahrendorf M, Pittet MJ. Imaging macrophages with nanoparticles. Nat Mater 2014;13(2):125–138.

58. Liu CH, Ren JQ, You Z, et al. Noninvasive detection of neural progenitor cells in living brains by MRI. FASEB J 2012;26(4):1652–1662.

59. Smith BR, Kempen P, Bouley D, et al. Shape matters: intravital microscopy reveals surprising geometrical dependence for nanoparticles in tumor models of extravasation. Nano Lett 2012;12(7):3369–3377.

60. Castaneda RT, Khurana A, Khan R, Daldrup-Link HE. Labeling stem cells with ferumoxytol, an FDA-approved iron oxide nanoparticle. J Vis Exp 2011;(57):e3482.

61. Henning TD, Wendland MF, Golovko D, et al. Relaxation effects of ferucarbotran-labeled mesenchymal stem cells at 1.5T and 3T: discrimination of viable from lysed cells. Magn Reson Med 2009;62(2):325–332.

62. Nejadnik H, Ye D, Lenkov OD, et al. Magnetic resonance imaging of stem cell apoptosis in arthritic joints with a caspase activatable contrast agent. ACS Nano 2015;9(2):1150–1160.

63. Patel MR, Chang YF, Chen IY, et al. Longitudinal, noninvasive imaging of T-cell effector function and proliferation in living subjects. Cancer Res 2010;70(24):10141–10149.

64. Yaghoubi SS, Jensen MC, Satyamurthy N, et al. Noninvasive detection of therapeutic cytolytic T cells with 18F-FHBG PET in a patient with glioma. Nat Clin Pract Oncol 2009;6(1):53–58.

65. Namavari M, Chang YF, Kusler B, Yaghoubi S, Mitchell BS, Gambhir SS. Synthesis of 2′-deoxy-2′-[18F]fluoro-9-β-D-arabinofuranosylguanine: a novel agent for imaging T-cell activation with PET. Mol Imaging Biol 2011;13(5):812–818.

66. Ye D, Liang G, Ma ML, Rao J. Controlling intracellular macrocyclization for the imaging of protease activity. Angew Chem Int Ed Engl 2011;50(10):2275–2279.

67. Razgulin A, Ma N, Rao J. Strategies for in vivo imaging of enzyme activity: an overview and recent advances. Chem Soc Rev 2011;40(7):4186–4216.

68. Liang G, Ren H, Rao J. A biocompatible condensation reaction for controlled assembly of nanostructures in living cells. Nat Chem 2010;2(1):54–60.

69. Daldrup-Link HE, Brasch RC. Macromolecular contrast agents for MR mammography: current status. Eur Radiol 2003;13(2):354–365.

70. Daldrup-Link HE, Henning T, Link TM. MR imaging of therapy-induced changes of bone marrow. Eur Radiol 2007;17(3):743–761.

71. Daldrup-Link HE, Kaiser A, Helbich T, et al. Macromolecular contrast medium (feruglose) versus small molecular contrast medium (gadopentetate) enhanced magnetic resonance imaging: differentiation of benign and malignant breast lesions. Acad Radiol 2003;10(11):1237–1246.

72. Daldrup-Link HE, Rummeny EJ, Ihssen B, Kienast J, Link TM. Iron-oxide-enhanced MR imaging of bone marrow in patients with non-Hodgkin's lymphoma: differentiation between tumor infiltration and hypercellular bone marrow. Eur Radiol 2002;12(6):1557–1566.

73. Daldrup-Link HE, Rydland J, Helbich TH, et al. Quantification of breast tumor microvascular permeability with feruglose-enhanced MR imaging: initial phase II multicenter trial. Radiology 2003;229(3):885–892.

74. Metz S, Lohr S, Settles M, et al. Ferumoxtran-10-enhanced MR imaging of the bone marrow before and after conditioning therapy in patients with non-Hodgkin lymphomas. Eur Radiol 2006;16(3):598–607.

75. Reimer P, Rummeny EJ, Daldrup HE, et al. Clinical results with Resovist: a phase 2 clinical trial. Radiology 1995;195(2):489–496.

76. Reimer P, Rummeny EJ, Daldrup HE, et al. Enhancement characteristics of liver metastases, hepatocellular carcinomas, and hemangiomas with Gd-EOB-DTPA: preliminary results with dynamic MR imaging. Eur Radiol 1997;7(2):275–280.

77. Simon G, Link TM, Wörtler K, et al. Detection of hepatocellular carcinoma: comparison of Gd-DTPA- and ferumoxides-enhanced MR imaging. Eur Radiol 2005;15(5):895–903.

78. Corot C, Robert P, Idée JM, Port M. Recent advances in iron oxide nanocrystal technology for medical imaging. Adv Drug Deliv Rev 2006;58(14):1471–1504.

79. Spinowitz BS, Schwenk MH, Jacobs PM, et al. The safety and efficacy of ferumoxytol therapy in anemic chronic kidney disease patients. Kidney Int 2005;68(4):1801–1807.

80. Lu M, Cohen MH, Rieves D, Pazdur R. FDA report: ferumoxytol for intravenous iron therapy in adult patients with chronic kidney disease. Am J Hematol 2010;85(5):315–319.

81. Ankrum JA, Ong JF, Karp JM. Mesenchymal stem cells: immune evasive, not immune privileged. Nat Biotechnol 2014;32(3):252–260.